Journal of Thermal Analysis and Calorimetry (2019) 137:1939–1949
https://doi.org/10.1007/s10973-019-08110-1

Darcy–Forchheimer flow of carbon nanotubes due to a convectively heated rotating disk with homogeneous–heterogeneous reactions

Tasawar Hayat[1,2] · Farwa Haider[1] · Taseer Muhammad[3] · Bashir Ahmad[2]

Received: 6 August 2018 / Accepted: 15 February 2019 / Published online: 2 March 2019

Abstract
Here, Darcy–Forchheimer flow of dissipating SWCNT and MWCNT nanofluids induced by rotation of disk with homogeneous–heterogeneous reactions and convective boundary condition is examined. Xue model of nanofluid is implemented in mathematical modeling. The resulting problems are computed for convergent optimal series solutions. Graphical results have been presented for physical quantities. Our findings indicate that skin friction coefficients and local Nusselt number are enhanced for larger values of nanoparticle volume fraction.

Keywords CNTs (SWCNTs and MWCNTs) · Darcy–Forchheimer flow · Homogeneous–heterogeneous reactions · Convective boundary condition · Rotating disk · OHAM

Introduction

The continuing interest of researchers in fluid flow by rotation of disk is because of its widespread geophysical and engineering applications such as centrifugal machinery, crystal growth process, pumping of metals at high melting point, thermal power generating systems, air cleaning machines, spin coating, and turbo machinery. The flow generated by the rotation of disk is interpreted by Von Karman [1]. Combined heat and mass transfer effects in flow induced by rotation of rough porous disk are analyzed by Turkyilmazoglu and Senel [2]. Rashidi et al. [3] scrutinized entropy generation due to slip flow of viscous liquid induced by a rotating porous disk with MHD. Nanofluid flow by rotation of disk is scrutinized by Turkyilmazoglu [4]. Hatami et al. [5] reported asymmetric laminar flow and heat transfer of viscous nanofluid between contraction and rotation of disks. They employed least square approach for solution development. Mustafa et al. [6] investigated nanofluid flow due to a stretching disk. It has been explored that uniform stretching of disk plays a substantial part in reduction in boundary layer thickness. Sheikholeslami et al. [7] discussed the numerical solution for the nanofluid deposition on an inclined rotating disk. Khan et al. [8] presented a numerical study for nanofluid flow caused by the rotation of disk employing Buongiorno's model. Partial slip flow of water-based nanofluids near a convectively heated stretchable rotating disk with MHD is elaborated by Mustafa and Khan [9]. Recently, Hayat et al. [10] scrutinized partial slip effect in MHD flow of viscous nanofluid by rotation of disk.

Carbon nanotube is a nano-sized cylinder of carbon atom with nanometer in diameter and several millimeters in length. Applications of carbon nanotubes CNTs in electrical and electrical applications include sensors, conductors, energy conversion devices, displays, photovoltaics, field-effect transistors, field emission display, supercapacitors, semiconductor devices, smart textiles, and several others. Enhancement in effective thermal conductivity of oil-based nanotube suspension is studied by Choi et al. [11]. Highest thermal conductivity enhancement is observed for nanotubes in comparison with other nanostructured materials dispersed in fluids. Ramasubramaniam et al. [12] illustrated

✉ Taseer Muhammad
taseer_qau@yahoo.com; taseer@gcwus.edu.pk

1 Department of Mathematics, Quaid-I-Azam University, Islamabad 44000, Pakistan

2 Nonlinear Analysis and Applied Mathematics (NAAM) Research Group, Department of Mathematics, Faculty of Science, King Abdulaziz University, Jeddah 21589, Saudi Arabia

3 Department of Mathematics, Government College Women University, Sialkot 51310, Pakistan

electrical applications of homogeneous carbon nanotube/polymer composite. A model which is valid for transport properties of carbon nanotubes-based composites is provided by Xue [13]. Heat transfer behavior by considering aqueous suspensions of multi-wall carbon nanotube flowing through a horizontal tube is explained by Ding et al. [14]. Numerical solution of heat transfer enhancement of multi-wall carbon nanotube is discussed by Kamali and Binesh [15]. Thermal transfer of carbon nanotubes in horizontal circular tube is investigated by Wang et al. [16]. The turbulent forced convection heat transfer of a functionalized multi-wall carbon nanotubes over a forward facing step is given by Safaei et al. [17]. Hayat et al. [18] analyzed stagnation point flow of water-based carbon nanotubes toward an impermeable stretching cylinder in the presence of homogeneous–heterogeneous reactions. Ellahi et al. [19] interpreted natural convective MHD flow of carbon nanotube along vertical cone. Karimipour et al. [20] utilized uniform heat flux for magnetic field and slip effects in laminar forced convection of water-based FMWNT carbon nanotubes in microchannels. Flow of nanofluids with different base fluids by an impermeable nonlinear stretchable surface with homogeneous–heterogeneous reactions and variable surface thickness is scrutinized by Hayat et al. [21]. Imtiaz et al. [22] explained thermal radiation effects in convective flow of water-based carbon nanotubes between stretchable rotating disks. Kandasamy et al. [23] elaborated combined effects of variable stream conditions and thermal radiation in magnetohydrodynamic unsteady flow of nanofluid over a porous wedge. Khan et al. [24] examined three-dimensional squeezing flow of nanofluid in a channel. Thermal performance of dissipating SWCNTs and MWCNTs between two concentric cylinders is described by Haq et al. [25]. Hayat et al. [26] investigated flow of dissipating SWCNTs and MWCNTs with porous space governed by Darcy–Forchheimer relation by rotating disk. Further recent investigations on nanofluids can be quoted through the studies [27–40].

Study and modeling of nonlinear flows through porous space is prominent area of research due to its enormous range of implications in geophysical, environmental, and industrial problems such as solar power, utilization of geothermal energy, chemical catalytic reactors, dryness of a porous solid, and the design of nuclear reactors. In 1856, Darcy presented a law which states that volumetric flux of fluid through medium is linearly proportional to pressure gradient. Inertia and boundary effects are neglected in classical Darcy's law. As the velocity increases, the flow becomes nonlinear and thus we cannot neglect porous inertia effects. Thus, Forchheimer [41] accounted such affects by considering a quadratic term in momentum equation. Muskat [42] demonstrated this law is valid for high Reynolds number. Seddeek [43] investigated mixed convection flow about an isothermal vertical flat plate embedded in fluid-saturated porous space. Jha and Kaurangini [44] provided approximate analytical solutions for flow in parallel plates channel with porous space governed by Brinkman–Forchheimer-extended Darcy relation. Some recent researches on Darcy–Forchheimer flow can be seen in the investigations [45–52].

Several chemically reacting structures involve homogeneous–heterogeneous reactions such as catalysis, combustion, hydrometallurgical devices, biochemical systems, production of ceramics, and distillation processes. At different rates, homogeneous and heterogeneous reactions have a complex correlation. Chemical reactions are utilized in hydrometallurgical industry, hardware configuration, crops damaging through freezing, mist development and scattering, orchards of fruit trees, and several others. Merkin [53] interpret effects of homogeneous–heterogeneous reactions in boundary layer flow of viscous fluid over a flat surface. Further advancements about homogeneous–heterogeneous reactions are seen in studies [54–61].

Main intention of current investigation is to interpret homogeneous–heterogeneous reactions in flow of SWCNTs and MWCNTs with porous space governed by Darcy–Forchheimer relation. Flow is induced by a convectively heated rotating disk using Xue [13] model. Optimal homotopy analysis method (OHAM) [62–70] is utilized for convergent series solutions. Effects of several influential parameters on physical quantities of interest are analyzed.

Model development

Convective flow of carbon nanotubes in porous space by rotation of disk is in the presence of homogeneous–heterogeneous reactions considered. It is assumed that flow is steady, incompressible, and axially symmetric and is placed at $z = 0$. Here, velocity components in directions of increasing (r, φ, z) are (u, v, w) (see Fig. 1). Surface is convectively heated featured by coefficient of heat transfer h_f and hot fluid temperature T_f. For cubic catalysis, homogeneous reaction is [58]:

$$A + 2B \rightarrow 3B, \quad \text{rate} = k_c a b^2. \tag{1}$$

Heterogeneous reaction at catalyst surface is

$$A \rightarrow B, \quad \text{rate} = k_s a, \tag{2}$$

in which chemical species A and B have rate constants k_c and k_s with concentrations a and b. Resulting expressions for 3D flow of carbon nanotubes in the absence of thermal radiation are [26, 58]:

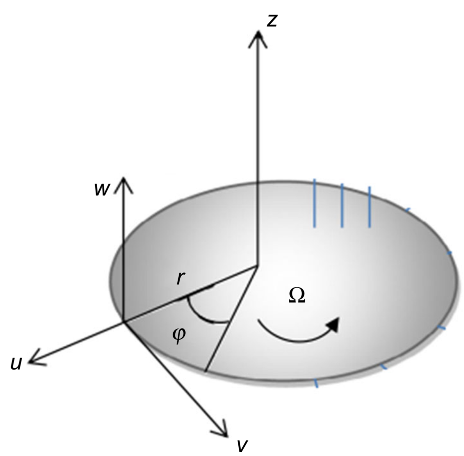

Fig. 1 Flow configuration

$$\frac{\partial u}{\partial r}+\frac{u}{r}+\frac{\partial w}{\partial z}=0, \tag{3}$$

$$u\frac{\partial u}{\partial r}-\frac{v^2}{r}+w\frac{\partial u}{\partial z}=\nu_{\rm nf}\left(\frac{\partial^2 u}{\partial r^2}+\frac{1}{r}\frac{\partial u}{\partial r}-\frac{u}{r^2}+\frac{\partial^2 u}{\partial z^2}\right)-\frac{\nu_{\rm nf}}{K^*}u - F^* u^2, \tag{4}$$

$$u\frac{\partial v}{\partial r}+\frac{uv}{r}+w\frac{\partial v}{\partial z}=\nu_{\rm nf}\left(\frac{\partial^2 v}{\partial r^2}+\frac{1}{r}\frac{\partial v}{\partial r}-\frac{v}{r^2}+\frac{\partial^2 v}{\partial z^2}\right) -\frac{\nu_{\rm nf}}{K^*}v-F^*v^2, \tag{5}$$

$$u\frac{\partial w}{\partial r}+w\frac{\partial w}{\partial z}=\nu_{\rm nf}\left(\frac{\partial^2 w}{\partial r^2}+\frac{1}{r}\frac{\partial w}{\partial r}+\frac{\partial^2 w}{\partial z^2}\right)-\frac{\nu_{\rm nf}}{K^*}w-F^*w^2, \tag{6}$$

$$u\frac{\partial T}{\partial r}+w\frac{\partial T}{\partial z}=\alpha_{\rm nf}\left(\frac{\partial^2 T}{\partial r^2}+\frac{1}{r}\frac{\partial T}{\partial r}+\frac{\partial^2 T}{\partial z^2}\right), \tag{7}$$

$$u\frac{\partial a}{\partial r}+w\frac{\partial a}{\partial z}=D_{\rm A}\left(\frac{\partial^2 a}{\partial r^2}+\frac{1}{r}\frac{\partial a}{\partial r}+\frac{\partial^2 a}{\partial z^2}\right)-k_{\rm c}ab^2, \tag{8}$$

$$u\frac{\partial b}{\partial r}+w\frac{\partial b}{\partial z}=D_{\rm B}\left(\frac{\partial^2 b}{\partial r^2}+\frac{1}{r}\frac{\partial b}{\partial r}+\frac{\partial^2 b}{\partial z^2}\right)+k_{\rm c}ab^2, \tag{9}$$

$$u=0,\quad v=r\Omega,\quad w=0,\quad -k_{\rm nf}\frac{\partial T}{\partial z}=h_{\rm f}(T_{\rm f}-T), \quad D_{\rm A}\frac{\partial a}{\partial z}=k_{\rm s}a,\quad D_{\rm B}\frac{\partial b}{\partial z}=-k_{\rm s}a \text{ at } z=0, \tag{10}$$

$$u\to 0,\quad v\to 0,\quad T\to T_\infty,\quad a\to a_0,\quad b\to 0 \text{ as } z\to\infty. \tag{11}$$

Here, K^* stands for permeability of porous medium, $F^*=\frac{C_{\rm b}}{rK^{*1/2}}$ and $C_{\rm b}$ for non-uniform inertia coefficient of porous space and drag coefficient, T for the temperature, $\alpha_{\rm nf}$ for the nanofluid thermal diffusivity and T_∞ for the ambient fluid temperature. Analytical model recommended by Xue [13] satisfies:

$$\begin{aligned}&\mu_{\rm nf}=\frac{\mu_{\rm f}}{(1-\phi)^{2.5}},\quad \nu_{\rm nf}=\frac{\mu_{\rm nf}}{\rho_{\rm nf}},\quad \alpha_{\rm nf}=\frac{k_{\rm nf}}{(\rho c_{\rm p})_{\rm nf}},\\ &\rho_{\rm nf}=\rho_{\rm f}(1-\phi)+\rho_{\rm CNT}\phi,\\ &(\rho c_{\rm p})_{\rm nf}=(\rho c_{\rm p})_{\rm f}(1-\phi)+(\rho c_{\rm p})_{\rm CNT}\phi,\\ &\frac{k_{\rm nf}}{k_{\rm f}}=\frac{(1-\phi)+2\phi\frac{k_{\rm CNT}}{k_{\rm CNT}-k_{\rm f}}\ln\frac{k_{\rm CNT}+k_{\rm f}}{2k_{\rm f}}}{(1-\phi)+2\phi\frac{k_{\rm f}}{k_{\rm CNT}-k_{\rm f}}\ln\frac{k_{\rm CNT}+k_{\rm f}}{2k_{\rm f}}},\end{aligned} \tag{12}$$

where $\mu_{\rm nf}$ stands for nanofluid effective dynamic viscosity, ϕ for solid volume fraction of nanoparticles, $\mu_{\rm f}$ for base fluids dynamic viscosity, $\rho_{\rm nf}$ for density of nanofluid, $\rho_{\rm f}$ for base fluid density, $(\rho c_{\rm p})_{\rm nf}$ for nanofluid effective heat capacity, $\rho_{\rm CNT}$ for density of carbon nanotubes, $k_{\rm CNT}$ for thermal conductivity of CNTs and $k_{\rm f}$ for base fluid thermal conductivity. The thermophysical characteristics of water and CNTs are demonstrated in Table 1.

Considering

$$u=r\Omega F'(\zeta),\quad v=r\Omega G(\zeta),\quad w=-\sqrt{2\Omega\nu_{\rm f}}F(\zeta),$$
$$\Theta(\zeta)=\frac{T-T_\infty}{T_{\rm f}-T_\infty},\quad a=a_0\Phi(\zeta),\quad b=a_0H(\zeta),\quad \zeta=\sqrt{\frac{2\Omega}{\nu_{\rm f}}}z. \tag{13}$$

Expression (3) is trivially justified and Eqs. (4)–(12) yield

$$\frac{1}{(1-\phi)^{2.5}\left(1-\phi+\frac{\rho_{\rm CNT}}{\rho_{\rm f}}\phi\right)}(2F'''-\lambda F')+2FF''-F'^2+G^2-F_{\rm r}f'^2=0, \tag{14}$$

$$\frac{1}{(1-\phi)^{2.5}\left(1-\phi+\frac{\rho_{\rm CNT}}{\rho_{\rm f}}\phi\right)}(2G''-\lambda G)+2FG'-2F'G-F_{\rm r}G^2=0, \tag{15}$$

$$\frac{k_{\rm nf}}{k_{\rm f}\left(1-\phi+\frac{(\rho c_{\rm p})_{\rm CNT}}{(\rho c_{\rm p})_{\rm f}}\phi\right)}\Theta''+Pr\,F\Theta'=0, \tag{16}$$

$$\frac{1}{Sc}\Phi''+F\Phi'-K\Phi H^2=0, \tag{17}$$

Table 1 Thermophysical characteristics of water and CNTs

Physical properties	Water	Nanoparticles	
		SWCNTs	MWCNTs
ρ/kg m^{-3}	997.1	2600	1600
k/W mK^{-1}	0.613	6600	3000
$c_{\rm p}$/J kg^{-1} K^{-1}	4179	425	796

$$\frac{\delta}{Sc}H'' + FH' + K\Phi H^2 = 0, \tag{18}$$

$$\begin{aligned} &F = 0, \quad F' = 0, \quad G = 1, \quad \Theta' = -\frac{k_f}{k_{nf}}\gamma(1-\Theta), \\ &\Phi' = K_s\Phi, \quad \delta H' = -K_s\Phi \text{ at } \zeta = 0, \end{aligned} \tag{19}$$

$$\begin{aligned} &F' \to 0, \quad G \to 0, \quad \Theta \to 0, \quad \Phi \to 1, \\ &H \to 0 \text{ as } \zeta \to \infty. \end{aligned} \tag{20}$$

In above expressions, F_r stands for Forchheimer number, λ for porosity parameter, γ for Biot number, Sc for Schmidt number, Pr for Prandtl number, K_s for strength of heterogeneous reaction, δ for ratio of diffusion coefficients and K for strength of homogeneous reaction which are defined as:

$$\left.\begin{aligned} &\lambda = \tfrac{\nu_f}{\Omega K^*}, \quad F_r = \tfrac{C_b}{K^{*1/2}}, \quad \gamma = \tfrac{h_f}{k_f}\sqrt{\tfrac{\nu_f}{2\Omega}}, \quad Pr = \tfrac{\nu_f}{\alpha_f}, \\ &Sc = \tfrac{\nu_f}{D_A}, \quad K_s = \tfrac{k_s}{D_A}\sqrt{\tfrac{\nu_f}{2\Omega}}, \quad K = \tfrac{k_c a_0^2}{2\Omega}, \quad \delta = \tfrac{D_B}{D_A}. \end{aligned}\right\} \tag{21}$$

For $D_A = D_B$, we have $\delta = 1$ and thus

$$\Phi(\zeta) + H(\zeta) = 1. \tag{22}$$

Now Eqs. (17) and (18) yield

$$\frac{1}{Sc}\Phi'' + F\Phi' - K\Phi(1-\Phi)^2 = 0. \tag{23}$$

Subjected boundary conditions are

$$\Phi'(0) = K_s\Phi(0), \quad \Phi(\infty) \to 1. \tag{24}$$

Coefficients of skin friction and local Nusselt number are

$$\left.\begin{aligned} &(Re_r)^{1/2}C_F = \tfrac{1}{(1-\phi)^{5/2}}F''(0), \\ &(Re_r)^{1/2}C_G = \tfrac{1}{(1-\phi)^{5/2}}G'(0), \\ &(Re_r)^{-1/2}Nu = -\tfrac{k_{nf}}{k_f}\Theta'(0), \end{aligned}\right\} \tag{25}$$

where $Re_r = \frac{(\Omega r)r}{2\nu_f}$ stands for local rotational Reynolds number.

Solutions by OHAM

It has been observed that Eqs. (14)–(16) and (23) with boundary conditions (19), (20) and (24) are four nonlinear ordinary differential equations. In order to compute the solutions, we have employed optimal homotopy analysis method (OHAM). Auxiliary linear operators and initial guesses have been selected in the forms:

$$\begin{aligned} &F_0(\zeta) = 0, \quad G_0(\zeta) = e^{-\zeta}, \quad \Theta_0(\zeta) = \frac{\gamma}{\gamma + \frac{k_{nf}}{k_f}}e^{-\zeta}, \\ &\Phi_0(\zeta) = 1 - \frac{1}{2}e^{-K_s\zeta}, \end{aligned} \tag{26}$$

$$\begin{aligned} &L_F = \frac{d^3F}{d\zeta^3} - \frac{dF}{d\zeta}, \quad L_G = \frac{d^2G}{d\zeta^2} - G, \quad L_\Theta = \frac{d^2\Theta}{d\zeta^2} - \Theta, \\ &L_\Phi = \frac{d^2\Phi}{d\zeta^2} - \Phi. \end{aligned} \tag{27}$$

The above linear operators obey

$$\begin{aligned} &L_F\left[H_1^* + H_2^*e^{\zeta} + H_3^*e^{-\zeta}\right] = 0, \quad L_G\left[H_4^*e^{\zeta} + H_5^*e^{-\zeta}\right] = 0, \\ &L_\Theta\left[H_6^*e^{\zeta} + H_7^*e^{-\zeta}\right] = 0, \quad L_\Phi\left[H_8^*e^{\zeta} + H_9^*e^{-\zeta}\right] = 0, \end{aligned} \tag{28}$$

in which H_j^* (j = 1–9) depicts the arbitrary constants. In view of above linear operators, we can easily develop zeroth- and mth-order deformation problem by BVPH2.0 of Mathematica.

Optimal convergence control parameters

We have solved momentum, energy and concentration equations through BVPh2.0. These expressions contain $\hbar_F$, $\hbar_G$, $\hbar_\Theta$ and $\hbar_\Phi$ which play significant role in homotopic solutions. To obtain optimal values of $\hbar_F$, $\hbar_G$, $\hbar_\Theta$ and $\hbar_\Phi$, the optimal analysis through minimization process is employed for average squared residual errors as follows:

$$\varepsilon_m^F = \frac{1}{k+1}\sum_{j=0}^{k}\left[N_F\left(\sum_{i=0}^{m}\hat{F}(\zeta), \sum_{i=0}^{m}\hat{G}(\zeta)\right)_{\zeta=j\delta\zeta}\right]^2, \tag{29}$$

$$\varepsilon_m^G = \frac{1}{k+1}\sum_{j=0}^{k}\left[N_G\left(\sum_{i=0}^{m}\hat{F}(\zeta), \sum_{i=0}^{m}\hat{G}(\zeta)\right)_{\zeta=j\delta\zeta}\right]^2, \tag{30}$$

$$\varepsilon_m^\Theta = \frac{1}{k+1}\sum_{j=0}^{k}\left[N_\Theta\left(\sum_{i=0}^{m}\hat{F}(\zeta), \sum_{i=0}^{m}\hat{G}(\zeta), \sum_{i=0}^{m}\hat{\Theta}(\zeta)\right)_{\zeta=j\delta\zeta}\right]^2, \tag{31}$$

$$\varepsilon_m^\Phi = \frac{1}{k+1}\sum_{j=0}^{k}\left[N_\Phi\left(\sum_{i=0}^{m}\hat{F}(\zeta), \sum_{i=0}^{m}\hat{G}(\zeta), \sum_{i=0}^{m}\hat{\Phi}(\zeta)\right)_{\zeta=j\delta\zeta}\right]^2. \tag{32}$$

Following Liao [62]:

$$\varepsilon_m^T = \varepsilon_m^F + \varepsilon_m^G + \varepsilon_m^\Theta + \varepsilon_m^\Phi, \tag{33}$$

where ε_m^T stands for total squared residual error, $\delta\zeta = 0.5$ and $k = 20$. The optimal values of convergence control variables for SWCNTs–water at second order of deformations are $\hbar_F = -0.666682$, $\hbar_G = -0.63389$, $\hbar_\Theta = -0.565967$ and $\hbar_\Phi = -1.88552$ and total averaged squared residual error is $\varepsilon_m^T = 0.0247373$, while the optimal values of convergence control variables for MWCNTs–water are

$\hbar_F = -0.609874$, $\hbar_G = -0.581243$, $\hbar_\Theta = -0.604961$ and $\hbar_\Phi = -1.8844$ and total averaged squared residual error is $\varepsilon_m^T = 0.0296666$. Total residual error graphs in SWCNTs and MWCNTs cases are plotted in Figs. 2 and 3, respectively. The individual average squared residual errors in SWCNTs and MWCNTs cases are interpreted in Tables 2 and 3. For higher order of approximations, the averaged squared residual errors decrease.

Discussion

This section consists of contribution of various flow variables such as porosity parameter λ, Forchheimer number F_r, nanoparticle volume fraction ϕ, Biot number γ, strength of homogeneous reaction K, Schmidt number Sc and strength of heterogeneous reactions K_s on $F'(\zeta)$, $G(\zeta)$, $\Theta(\zeta)$ and $\Phi(\zeta)$. Figure 4 is plotted to explore the impact of porosity parameter λ on $F'(\zeta)$. Higher estimation of porosity parameter causes lower velocity field $F'(\zeta)$ for SWCNTs and MWCNTs cases. Figure 5 displays the variation in velocity $F'(\zeta)$ for various values of Forchheimer number F_r. An increment in Forchheimer number F_r causes lower velocity field $F'(\zeta)$ in SWCNTs and MWCNTs cases. Figure 6 shows that larger nanoparticle volume fraction ϕ produces stronger velocity field $F'(\zeta)$ for SWCNTs and MWCNTs cases. Figure 7 scrutinizes that velocity field $G(\zeta)$ shows decreasing trend via larger porosity parameter λ in SWCNTs and MWCNTs cases. Higher Forchheimer number F_r constitutes a decrement in velocity field $G(\zeta)$ in SWCNTs and MWCNTs cases (see Fig. 8). An increment in $G(\zeta)$ is occurred for larger ϕ for both SWCNTs and MWCNTs cases (see Fig. 9). Figure 10 is sketched to elaborate the influence of porosity parameter λ on $\Theta(\zeta)$. By an increment in porosity parameter λ, the temperature $\Theta(\zeta)$ enhances in SWCNTs and MWCNTs cases. Figure 11 reveals the features of Forchheimer number F_r on $\Theta(\zeta)$. Larger Forchheimer number F_r produces higher-temperature field $\Theta(\zeta)$ in SWCNTs and MWCNTs cases. Figure 12 shows that by increasing ϕ, stronger $\Theta(\zeta)$ is generated in SWCNTs and MWCNTs cases. Figure 13 is drawn to scrutinize that how $\Theta(\zeta)$ is affected with variation in Biot number γ. By increasing Biot number γ, strong convection produces which causes higher-temperature $\Theta(\zeta)$ in SWCNTs and MWCNTs cases. Higher estimation of porosity parameter λ leads to weaker concentration field $\Phi(\zeta)$ in SWCNTs and MWCNTs cases

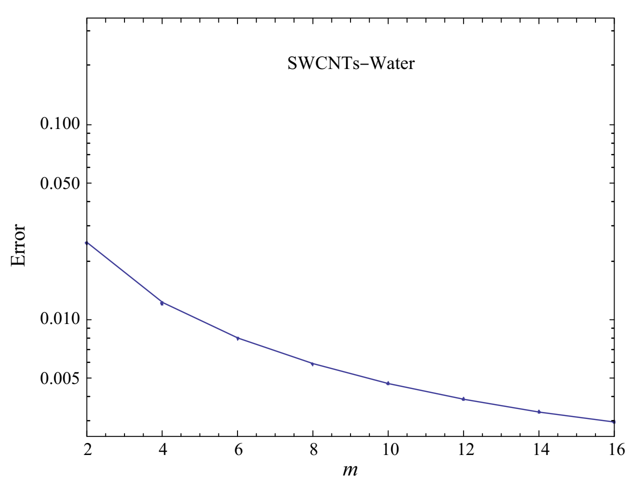

Fig. 2 Plots of total residual error in SWCNTs–water

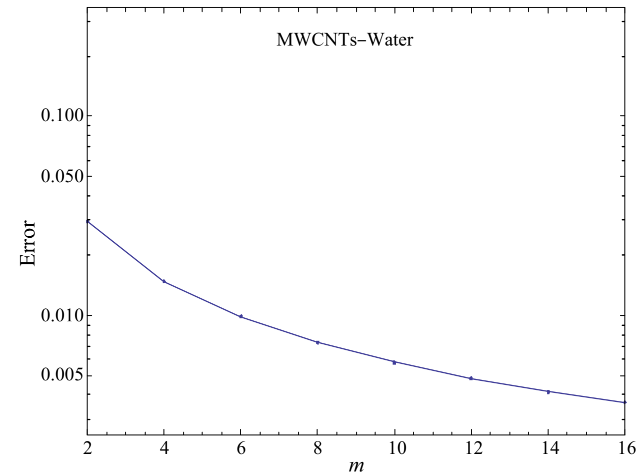

Fig. 3 Plots of total residual error in MWCNTs–water

Table 2 Individual averaged squared residual errors in view of optimal data of auxiliary parameters in SWCNTs–water case

m	ε_m^F	ε_m^G	ε_m^Θ	ε_m^Φ
2	3.56×10^{-3}	1.81×10^{-2}	2.07×10^{-3}	9.91×10^{-4}
6	1.23×10^{-3}	4.65×10^{-3}	1.55×10^{-3}	5.26×10^{-4}
10	6.88×10^{-4}	2.27×10^{-3}	1.38×10^{-3}	3.48×10^{-4}
14	4.42×10^{-4}	1.38×10^{-3}	1.29×10^{-3}	2.57×10^{-4}
16	3.67×10^{-4}	1.14×10^{-3}	1.25×10^{-3}	2.27×10^{-4}

Table 3 Individual averaged squared residual errors in view of optimal data of auxiliary parameters in MWCNTs–water case

m	ε_m^F	ε_m^G	ε_m^Θ	ε_m^Φ
2	3.64×10^{-3}	2.30×10^{-2}	2.01×10^{-3}	1.01×10^{-3}
6	1.36×10^{-3}	6.41×10^{-3}	1.49×10^{-3}	5.58×10^{-4}
10	8.13×10^{-4}	3.29×10^{-3}	1.33×10^{-3}	3.78×10^{-4}
14	5.48×10^{-4}	2.07×10^{-3}	1.24×10^{-3}	2.83×10^{-4}
16	4.65×10^{-4}	1.72×10^{-3}	1.20×10^{-3}	2.50×10^{-4}

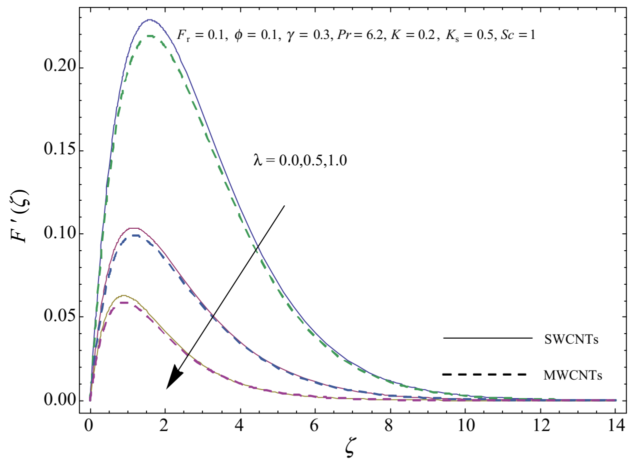

Fig. 4 Plots of $F'(\zeta)$ for λ

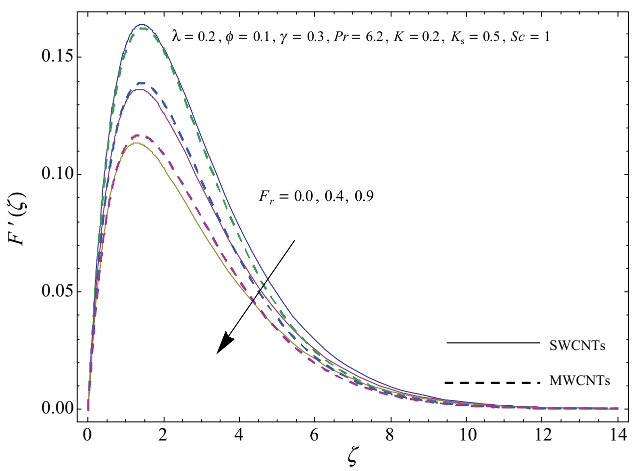

Fig. 5 Plots of $F'(\zeta)$ for F_r

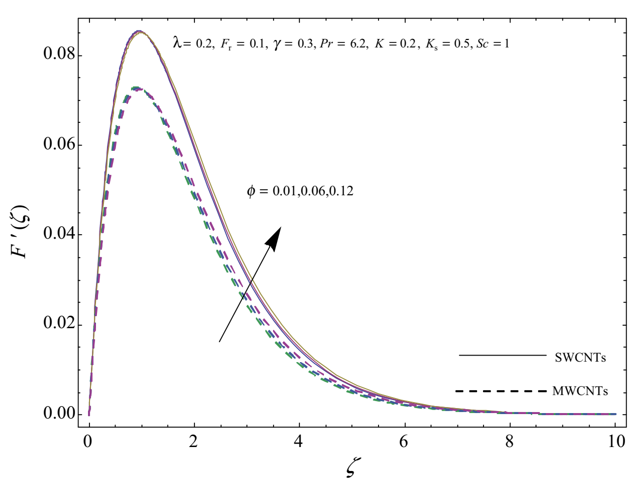

Fig. 6 Plots of $F'(\zeta)$ for ϕ

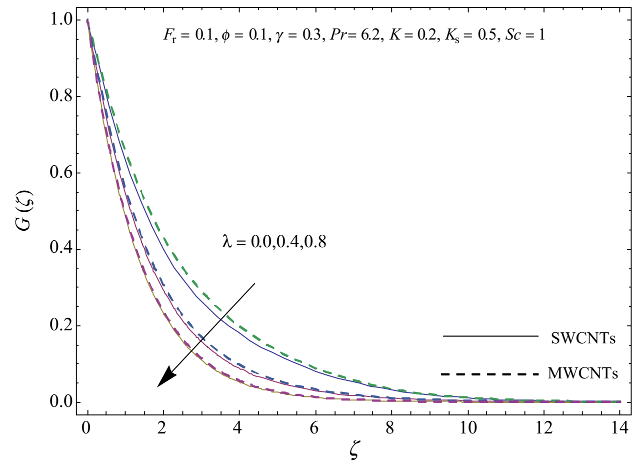

Fig. 7 Plots of $G(\zeta)$ for λ

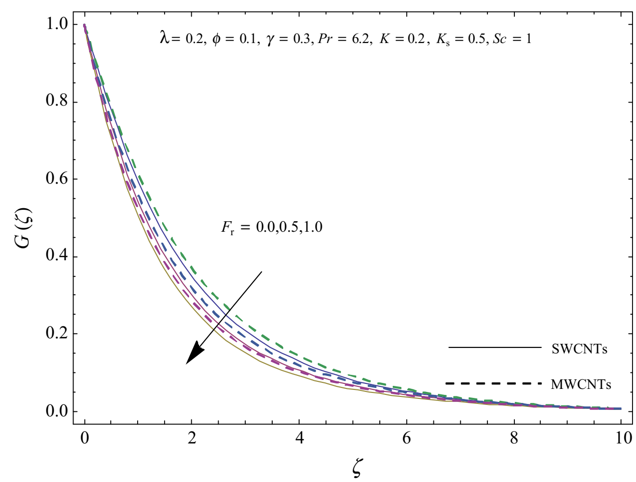

Fig. 8 Plots of $G(\zeta)$ for F_r

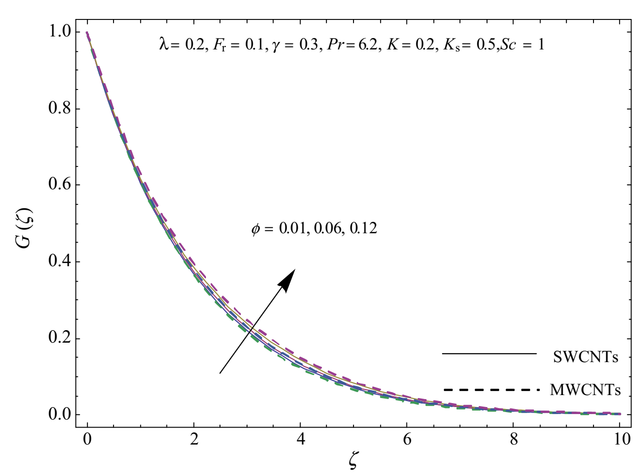

Fig. 9 Plots of $G(\zeta)$ for ϕ

(see Fig. 14). Figure 15 interprets that $\Phi(\zeta)$ and related layer thickness show decreasing trend for increasing F_r. Behavior of ϕ on concentration field $\Phi(\zeta)$ is presented in Fig. 16. Larger ϕ corresponds to increasing trend in the concentration field $\Phi(\zeta)$ in SWCNTs and MWCNTs cases. Figure 17 presents the variation in $\Phi(\zeta)$ for distinct values

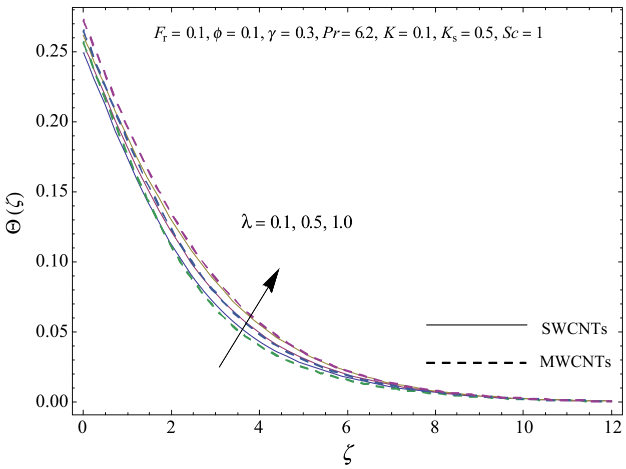

Fig. 10 Plots of $\Theta(\zeta)$ for λ

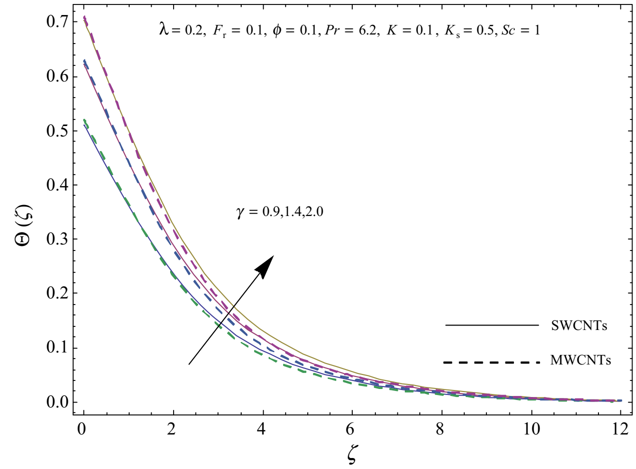

Fig. 13 Plots of $\Theta(\zeta)$ for γ

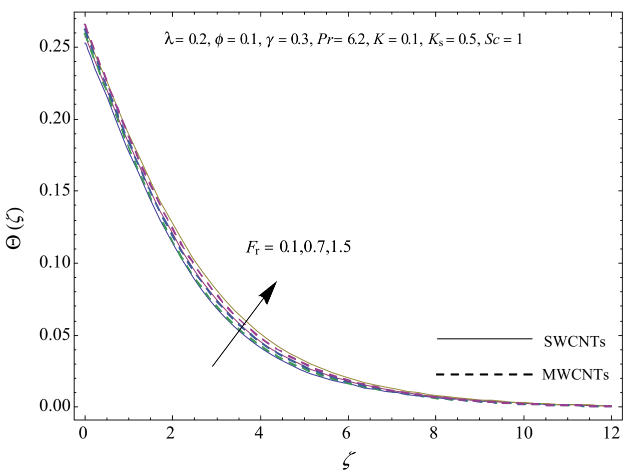

Fig. 11 Plots of $\Theta(\zeta)$ for F_r

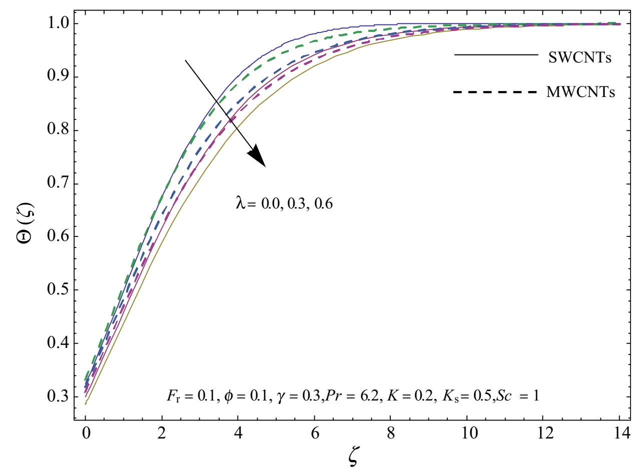

Fig. 14 Plots of $\Phi(\zeta)$ for λ

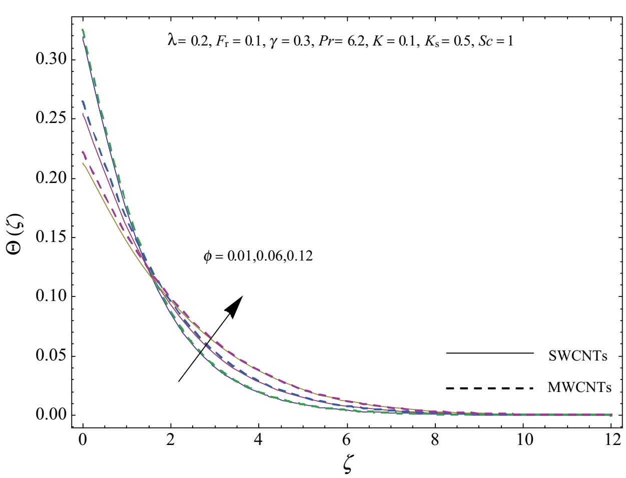

Fig. 12 Plots of $\Theta(\zeta)$ for ϕ

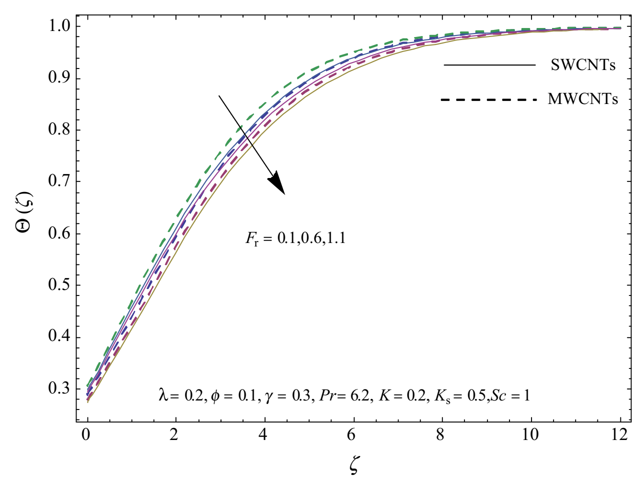

Fig. 15 Plots of $\Phi(\zeta)$ for F_r

of K. An increase in K corresponds to lower $\Phi(\zeta)$ in SWCNTs and MWCNTs cases. Figure 18 presents the curves of concentration $\Phi(\zeta)$ for distinct values of K_s. By enhancing strength of heterogeneous reaction K_s, diffusion reduces which enhances the concentration $\Phi(\zeta)$ in

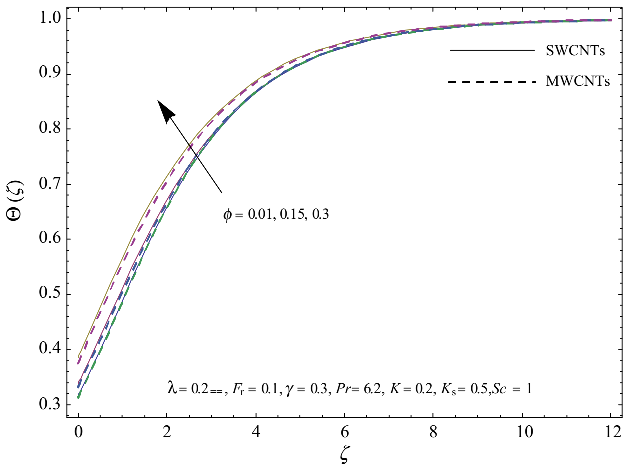

Fig. 16 Plots of $\Phi(\zeta)$ for ϕ

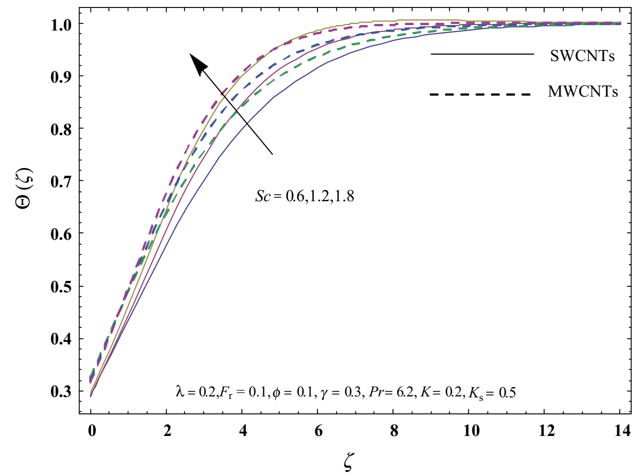

Fig. 19 Plots of $\Phi(\zeta)$ for Sc

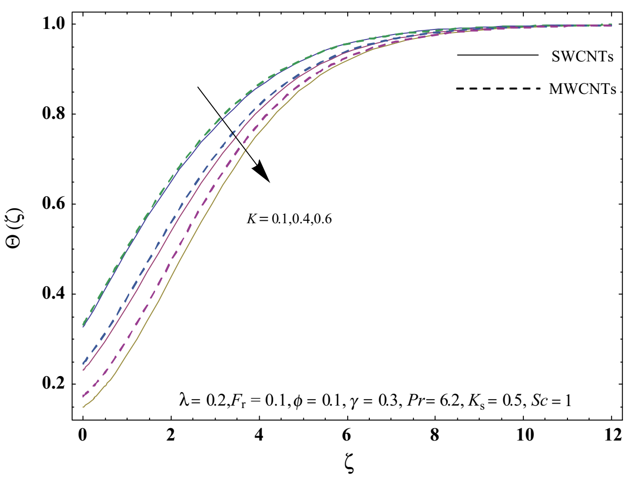

Fig. 17 Plots of $\Phi(\zeta)$ for K

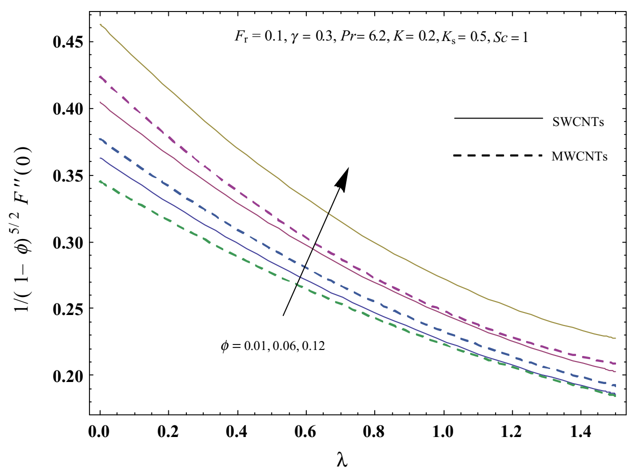

Fig. 20 Plots of $(1/(1-\phi)^{5/2})F''(0)$ for ϕ and λ

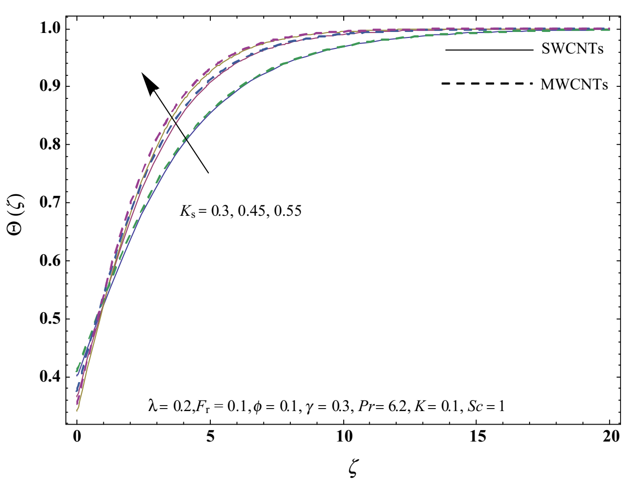

Fig. 18 Plots of $\Phi(\zeta)$ for K_s

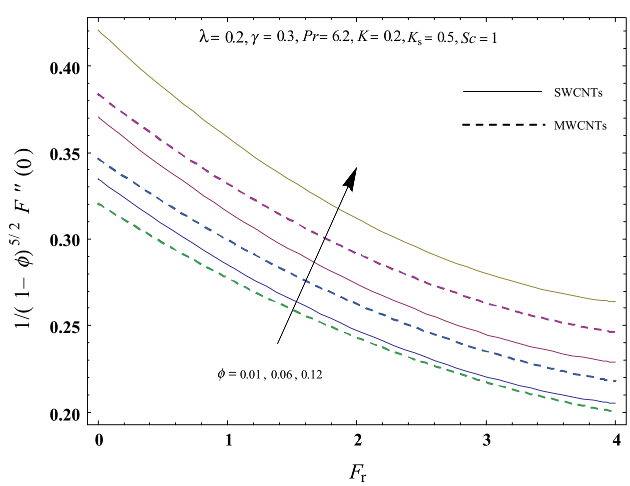

Fig. 21 Plots of $(1/(1-\phi)^{5/2})F''(0)$ for ϕ and F_r

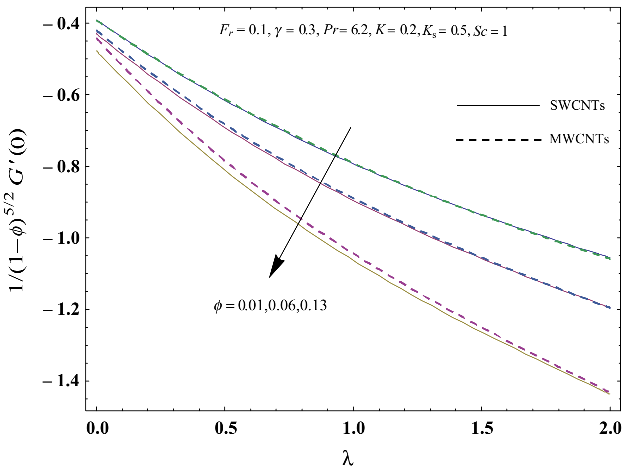

Fig. 22 Plots of $(1/(1-\phi)^{5/2})G'(0)$ for ϕ and λ

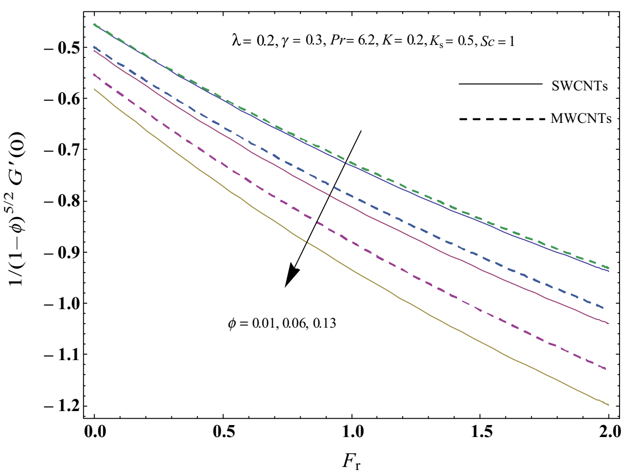

Fig. 23 Plots of $(1/(1-\phi)^{5/2})G'(0)$ for ϕ and F_r

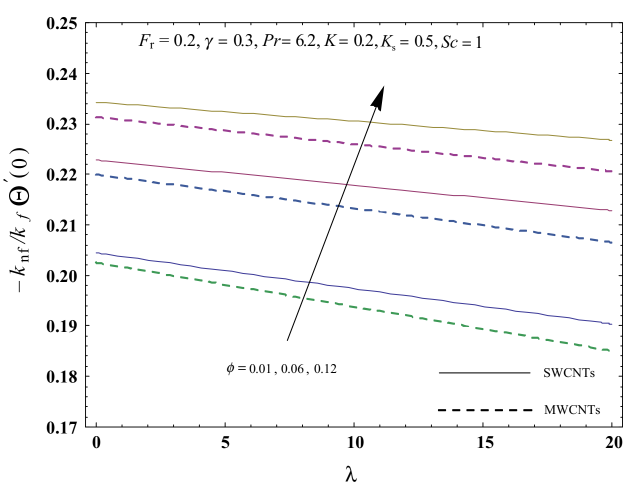

Fig. 24 Plots of $-(k_{nf}/k_f)\Theta'(0)$ for ϕ and λ

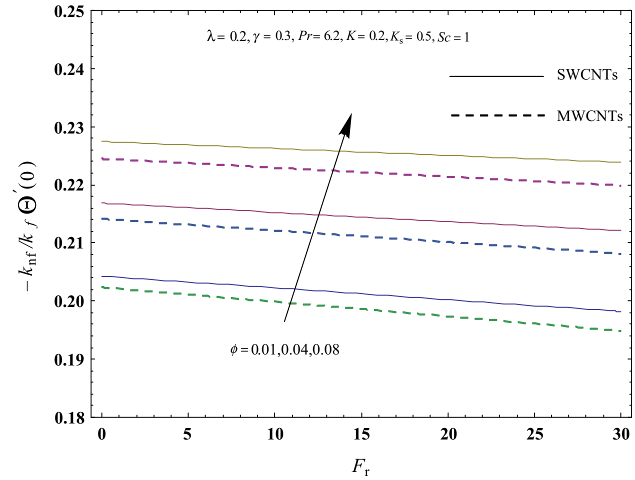

Fig. 25 Plots of $-(k_{nf}/k_f)\Theta'(0)$ for ϕ and F_r

SWCNTs and MWCNTs cases. More concentration $\Phi(\zeta)$ is noted for higher Schmidt number Sc (see Fig. 19). Figures 20–23 depict the skin friction coefficients $\left(1/(1-\phi)^{5/2}\right)F''(0)$ and $\left(1/(1-\phi)^{5/2}\right)G'(0)$ for various values of ϕ, λ and F_r. It has been reported that for both SWCNTs and MWCNTs, skin friction coefficients are enhanced for larger values of ϕ. Figures 24 and 25 elucidate that local Nusselt number is enhanced for higher ϕ in SWCNTs and MWCNTs cases.

Conclusions

Convective flow of water-based carbon nanotubes by rotating disk with Darcy–Forchheimer relation and homogeneous–heterogeneous reactions has been discussed. Main results are summarized as:

- An increase in nanoparticle volume fraction ϕ presents higher velocities $F'(\zeta)$ and $G(\zeta)$.
- Both $\Theta(\zeta)$ and $\Phi(\zeta)$ are increasing functions of nanoparticle volume fraction ϕ.
- Higher porosity parameter λ and Forchheimer number F_r yield stronger temperature $\Theta(\zeta)$ field while opposite behavior is observed for concentration $\Phi(\zeta)$.
- Larger K_s and Schmidt number Sc show stronger concentration field $\Phi(\zeta)$.
- Enhancement in temperature $\Theta(\zeta)$ is anticipated for higher Biot number γ.
- Concentration $\Phi(\zeta)$ is reduced for larger strength of homogeneous reaction K.
- Higher estimation of porosity parameter λ and Forchheimer number F_r yield higher skin friction coefficients.
- Heat transfer rate is enhanced for increasing values of porosity parameter λ and Forchheimer number F_r.

References

1. Von Karman T. Uber laminare and turbulente Reibung. ZAMM Z Angew Math Mech. 1921;1:233–52.
2. Turkyilmazoglu M, Senel P. Heat and mass transfer of the flow due to a rotating rough and porous disk. Int J Therm Sci. 2013;63:146–58.
3. Rashidi MM, Kavyani N, Abelman S. Investigation of entropy generation in MHD and slip flow over rotating porous disk with variable properties. Int J Heat Mass Transf. 2014;70:892–917.
4. Turkyilmazoglu M. Nanofluid flow and heat transfer due to a rotating disk. Comput Fluids. 2014;94:139–46.
5. Hatami M, Sheikholeslami M, Gangi DD. Laminar flow and heat transfer of nanofluids between contracting and rotating disks by least square method. Power Technol. 2014;253:769–79.
6. Mustafa M, Khan JA, Hayat T, Alsaedi A. On Bödewadt flow and heat transfer of nanofluids over a stretching stationary disk. J Mol Liq. 2015;211:119–25.
7. Sheikholeslami M, Hatami M, Ganji DD. Numerical investigation of nanofluid spraying on an inclined rotating disk for cooling process. J Mol Liq. 2015;211:577–83.
8. Khan JA, Mustafa M, Hayat T, Turkyilmazoglu M, Alsaedi A. Numerical study of nanofluid flow and heat transfer over a rotating disk using Buongiorno's model. Int J Numer Methods Heat Fluid Flow. 2017;27:221–34.
9. Mustafa M, Khan JA. Numerical study of partial slip effects on MHD flow of nanofluids near a convectively heated stretchable rotating disk. J Mol Liq. 2017;234:287–95.
10. Hayat T, Muhammad T, Shehzad SA, Alsaedi A. On magnetohydrodynamic flow of nanofluid due to a rotating disk with slip effect: a numerical study. Comput Methods Appl Mech Eng. 2017;315:467–77.
11. Choi SUS, Zhang ZG, Yu W, Lockwood FE, Grulke EA. Anomalous thermal conductivity enhancement in nanotube suspensions. Appl Phys Lett. 2001;79:2252.
12. Ramasubramaniam R, Chen J, Liu H. Homogeneous carbon nanotube/polymer composites for electrical applications. Appl Phys Lett. 2003;83:2928.
13. Xue QZ. Model for thermal conductivity of carbon nanotube-based composites. Physica B. 2005;368:302–7.
14. Ding Y, Alias H, Wen D, Williams RA. Heat transfer of aqueous suspensions of carbon nanotubes (CNT nanofluids). Int J Heat Mass Transf. 2006;49:240–50.
15. Kamali R, Binesh A. Numerical investigation of heat transfer enhancement using carbon nanotube-based non-Newtonian nanofluids. Int Commun Heat Mass Transf. 2010;37:1153–7.
16. Wang J, Zhu J, Zhang X, Chen Y. Heat transfer and pressure drop of nanofluids containing carbon nanotubes in laminar flows. Exp Therm Fluid Sci. 2013;44:716–21.
17. Safaei MR, Togun H, Vafai K, Kazi SN, Badarudin A. Investigation of heat transfer enhancement in a forward-facing contracting channel using FMWCNT nanofluids. Numer Heat Transf Part A. 2014;66:1321–40.
18. Hayat T, Farooq M, Alsaedi A. Homogeneous–heterogeneous reactions in the stagnation point flow of carbon nanotubes with Newtonian heating. AIP Adv. 2015;5:027130.
19. Ellahi R, Hassan M, Zeeshan A. Study of natural convection MHD nanofluid by means of single and multi walled carbon nanotubes suspended in a salt water solutions. IEEE Trans Nanotechnol. 2015;14:726–34.
20. Karimipour A, Taghipour A, Malvandi A. Developing the laminar MHD forced convection flow of water/FMWNT carbon nanotubes in a microchannel imposed the uniform heat flux. J Magn Magn Mater. 2016;419:420–8.
21. Hayat T, Hussain Z, Muhammad T, Alsaedi A. Effects of homogeneous and heterogeneous reactions in flow of nanofluids over a nonlinear stretching surface with variable surface thickness. J Mol Liq. 2016;21:1121–7.
22. Imtiaz M, Hayat T, Alsaedi A, Ahmad B. Convective flow of carbon nanotubes between rotating stretchable disks with thermal radiation effects. Int J Heat Mass Transf. 2016;101:948–57.
23. Kandasamy R, Muhaimin I, Mohammad R. Single walled carbon nanotubes on MHD unsteady flow over a porous wedge with thermal radiation with variable stream conditions. Alex Eng J. 2016;55:275–85.
24. Khan U, Ahmed N, Mohyud-Din ST. Numerical investigation for three dimensional squeezing flow of nanofluid in a rotating channel with lower stretching wall suspended by carbon nanotubes. Appl Therm Eng. 2017;113:1107–17.
25. Haq RU, Shahzad F, Al-Mdallal QM. MHD pulsatile flow of engine oil based carbon nanotubes between two concentric cylinders. Results Phys. 2017;7:57–68.
26. Hayat T, Haider F, Muhammad T, Alsaedi A. On Darcy-Forchheimer flow of carbon nanotubes due to a rotating disk. Int J Heat Mass Transf. 2017;112:248–54.
27. Turkyilmazoglu M. A note on the correspondence between certain nanofluid flows and standard fluid flows. J Heat Transf. 2015;137:024501.
28. Mahanthesh B, Gireesha BJ, PrasannaKumara BC, Shashikumar NS. Marangoni convection radiative flow of dusty nanoliquid with exponential space dependent heat source. Nucl Eng Technol. 2017;49:1660–8.
29. Mahanthesh B, Mabood F, Gireesha BJ, Gorla RSR. Effects of chemical reaction and partial slip on the three-dimensional flow of a nanofluid impinging on an exponentially stretching surface. Eur Phys J Plus. 2017;132:113.
30. Mahanthesh B, Gireesha BJ, Shashikumar NS, Shehzad SA. Marangoni convective MHD flow of SWCNT and MWCNT nanoliquids due to a disk with solar radiation and irregular heat source. Physica E. 2017;94:25–30.
31. Gireesha BJ, Mahanthesh B, Thammanna GT, Sampathkumar PB. Hall effects on dusty nanofluid two-phase transient flow past a stretching sheet using KVL model. J Mol Liq. 2018;256:139–47.
32. Mahanthesh B, Gireesha BJ, Gorla RSR, Makinde OD. Magnetohydrodynamic three-dimensional flow of nanofluids with slip and thermal radiation over a nonlinear stretching sheet: a numerical study. Neural Comput Appl. 2018;30:1557–67.
33. Kumar PBS, Mahanthesh B, Gireesha BJ, Shehzad SA. Quadratic convective flow of radiated nano-Jeffrey liquid subject to multiple convective conditions and Cattaneo–Christov double diffusion. Appl Math Mech. 2018;39:1311–26.
34. Muhammad T, Lu DC, Mahanthesh B, Eid MR, Ramzan M, Dar A. Significance of Darcy–Forchheimer porous medium in nanofluid through carbon nanotubes. Commun Theor Phys. 2018;70:361.
35. Sheikholeslami M, Hayat T, Muhammad T, Alsaedi A. MHD forced convection flow of nanofluid in a porous cavity with hot elliptic obstacle by means of Lattice Boltzmann method. Int J Mech Sci. 2018;135:532–40.
36. Hayat T, Aziz A, Muhammad T, Alsaedi A. An optimal analysis for Darcy–Forchheimer 3D flow of Carreau nanofluid with convectively heated surface. Results Phys. 2018;9:598–608.
37. Rashidi S, Mahian O, Languri EM. Applications of nanofluids in condensing and evaporating systems. J Therm Anal Calorim. 2018;131:2027–39.
38. Rashidi S, Eskandarian M, Mahian O, Poncet S. Combination of nanofluid and inserts for heat transfer enhancement. J Therm Anal Calorim. 2018. https://doi.org/10.1007/s10973-018-7070-9.

39. Hayat T, Aziz A, Muhammad T, Alsaedi A. Effects of binary chemical reaction and Arrhenius activation energy in Darcy-Forchheimer three-dimensional flow of nanofluid subject to rotating frame. J Therm Anal Calorim. 2018. https://doi.org/10.1007/s10973-018-7822-6.
40. Hayat T, Aziz A, Muhammad T, Alsaedi A. Numerical simulation for Darcy-Forchheimer three-dimensional rotating flow of nanofluid with prescribed heat and mass flux conditions. J Therm Anal Calorim. 2018. https://doi.org/10.1007/s10973-018-7847-x.
41. Forchheimer P. Wasserbewegung durch boden. Z Ver Dtsch Ing. 1901;45:1782–8.
42. Muskat M. The flow of homogeneous fluids through porous media. Ann Arbor: Edwards; 1946.
43. Seddeek MA. Influence of viscous dissipation and thermophoresis on Darcy–Forchheimer mixed convection in a fluid saturated porous media. J Colloid Interface Sci. 2006;293:137–42.
44. Jha BK, Kaurangini ML. Approximate analytical solutions for the nonlinear Brinkman–Forchheimer-extended Darcy flow model. Appl Math. 2011;2:1432–6.
45. Pal D, Mondal H. Hydromagnetic convective diffusion of species in Darcy–Forchheimer porous medium with non-uniform heat source/sink and variable viscosity. Int Commun Heat Mass Transf. 2012;39:913–7.
46. Sadiq MA, Hayat T. Darcy–Forchheimer flow of magneto Maxwell liquid bounded by convectively heated sheet. Results Phys. 2016;6:884–90.
47. Shehzad SA, Abbasi FM, Hayat T, Alsaedi A. Cattaneo–Christov heat flux model for Darcy–Forchheimer flow of an Oldroyd-B fluid with variable conductivity and non-linear convection. J Mol Liq. 2016;224:274–8.
48. Bakar SA, Arifin NM, Nazar R, Ali FM, Pop I. Forced convection boundary layer stagnation-point flow in Darcy–Forchheimer porous medium past a shrinking sheet. Front Heat Mass Transf. 2016;7:38.
49. Hayat T, Muhammad T, Al-Mezal S, Liao SJ. Darcy-Forchheimer flow with variable thermal conductivity and Cattaneo-Christov heat flux. Int J Numer Methods Heat Fluid Flow. 2016;26:2355–69.
50. Umavathi JC, Ojjela O, Vajravelu K. Numerical analysis of natural convective flow and heat transfer of nanofluids in a vertical rectangular duct using Darcy–Forchheimer–Brinkman model. Int J Therm Sci. 2017;111:511–24.
51. Hayat T, Haider F, Muhammad T, Alsaedi A. On Darcy–Forchheimer flow of viscoelastic nanofluids: a comparative study. J Mol Liq. 2017;233:278–87.
52. Muhammad T, Alsaedi A, Shehzad SA, Hayat T. A revised model for Darcy–Forchheimer flow of Maxwell nanofluid subject to convective boundary condition. Chin J Phys. 2017;55:963–76.
53. Merkin JH. A model for isothermal homogeneous–heterogeneous reactions in boundary-layer flow. Math Comput Model. 1996;24:125–36.
54. Chaudhary MA, Merkin JH. A simple isothermal model for homogeneous–heterogeneous reactions in boundary-layer flow. II Different diffusivities for reactant and autocatalyst. Fluid Dyn Res. 1995;16:335–59.
55. Bachok N, Ishak A, Pop I. On the stagnation-point flow towards a stretching sheet with homogeneous–heterogeneous reactions effects. Commun Nonlinear Sci Numer Simul. 2011;16:4296–302.
56. Kameswaran PK, Shaw S, Sibanda P, Murthy PVSN. Homogeneous–heterogeneous reactions in a nanofluid flow due to porous stretching sheet. Int J Heat Mass Transf. 2013;57:465–72.
57. Imtiaz M, Hayat T, Alsaedi A, Hobiny A. Homogeneous–heterogeneous reactions in MHD flow due to an unsteady curved stretching surface. J Mol Liq. 2016;221:245–53.
58. Abbas Z, Sheikh M. Numerical study of homogeneous–heterogeneous reactions on stagnation point flow of ferrofluid with non-linear slip condition. Chin J Chem Eng. 2017;25:11–7.
59. Sajid M, Iqbal SA, Naveed M, Abbas Z. Effect of homogeneous–heterogeneous reactions and magnetohydrodynamics on Fe_3O_4 nanofluid for the Blasius flow with thermal radiations. J Mol Liq. 2017;233:115–21.
60. Hayat T, Haider F, Muhammad T, Alsaedi A. Darcy–Forchheimer flow with Cattaneo–Christov heat flux and homogeneous–heterogeneous reactions. PLoS ONE. 2017;12:e0174938.
61. Hayat T, Sajjad R, Ellahi R, Alsaedi A, Muhammad T. Homogeneous–heterogeneous reactions in MHD flow of micropolar fluid by a curved stretching surface. J Mol Liq. 2017;240:209–20.
62. Liao SJ. An optimal homotopy-analysis approach for strongly nonlinear differential equations. Commun Nonlinear Sci Numer Simul. 2010;15:2003–16.
63. Malvandi A, Hedayati F, Domairry G. Stagnation point flow of a nanofluid toward an exponentially stretching sheet with nonuniform heat generation/absorption. J Thermodyn. 2013;2013:764827.
64. Abbasbandy S, Hayat T, Alsaedi A, Rashidi MM. Numerical and analytical solutions for Falkner–Skan flow of MHD Oldroyd-B fluid. Int J Numer Methods Heat Fluid Flow. 2014;24:390–401.
65. Hayat T, Muhammad T, Alsaedi A, Alhuthali MS. Magnetohydrodynamic three-dimensional flow of viscoelastic nanofluid in the presence of nonlinear thermal radiation. J Magn Magn Mater. 2015;385:222–9.
66. Hayat T, Aziz A, Muhammad T, Alsaedi A. On magnetohydrodynamic three-dimensional flow of nanofluid over a convectively heated nonlinear stretching surface. Int J Heat Mass Transf. 2016;100:566–72.
67. Turkyilmazoglu M. An effective approach for evaluation of the optimal convergence control parameter in the homotopy analysis method. Filomat. 2016;30:1633–50.
68. Hayat T, Aziz A, Muhammad T, Ahmad B. On magnetohydrodynamic flow of second grade nanofluid over a nonlinear stretching sheet. J Magn Magn Mater. 2016;408:99–106.
69. Hayat T, Muhammad T, Shehzad SA, Alsaedi A. An analytical solution for magnetohydrodynamic Oldroyd-B nanofluid flow induced by a stretching sheet with heat generation/absorption. Int J Therm Sci. 2017;111:274–88.
70. Hayat T, Ullah I, Muhammad T, Alsaedi A. Thermal and solutal stratification in mixed convection three-dimensional flow of an Oldroyd-B nanofluid. Results Phys. 2017;7:3797–805.